Acoustic logic networks realized with non-Hermitian and nonlocal metagratings

Hanjie Xiao,[1] Chuanxin Zhang,[1] Ying Li,[1,*] Dean Ta,[1,2] and Xue Jiang[1,2,†]

[1] *Department of Biomedical Engineering, School of Information Science and Technology, Fudan University, Shanghai, 200433, China*

[2] *State Key Laboratory of Integrated Chips and System, Fudan University, Shanghai, 200433, China*

(Received 5 June 2024; revised 22 July 2024; accepted 31 July 2024; published 16 August 2024)

This paper proposes the concept and demonstrates the realization of acoustic logic networks (ALNs), a system that performs various logic operations using sound waves. Unlike traditional systems with separate components, ALNs integrate multiple logic functionalities with a single platform, performing operations like AND, OR, and XOR gates, similar to those used in electronic computers. The design of ALNs leverages the non-Hermitian and nonlocal metagratings. By considering the intricate nonlocal interaction within the structure, the metagratings are designed to operate at exceptional points (EPs) to achieve the desired logic functions. Two metagratings are cascaded to construct the acoustic logic module (ALM), which acts as the basic building block of an ALN. The effectiveness of ALNs is confirmed through theoretical calculations, numerical simulations, and experiments. We demonstrate the ability to perform complex logic operations and realize various multichannel computing functions with the ALN of different configurations. These results showcase precise control over sound waves and significantly enhanced computing capabilities. The proposed ALNs represent a significant step forward in acoustic computing. This technology has the potential to revolutionize fields where traditional electronic computing might be impractical due to size, energy efficiency, or environmental limitations.

DOI: 10.1103/PhysRevApplied.22.024048

I. INTRODUCTION

The miniaturization and improvement of computing devices have driven significant research into new physical approaches for performing logical operations [1–3]. Sound waves present a particularly promising avenue due to their inherent advantages in scalability, energy efficiency, and compatibility with existing technologies [4–6]. Acoustic logic gates (ALGs), which use sound waves to carry out logical operations, represent a new frontier in this field. These gates leverage unique sound wave properties to offer a robust alternative to traditional electronic and optical logic mechanisms, positioning them at the forefront of emerging computational technologies [7–9]. Compared with optical logic gates, ALGs offer enhanced resilience to environmental disturbances. While optical components suffer significant attenuation in some conditions, acoustic systems display a remarkable ability to adapt to such attenuation, even utilizing it to engineer abnormal acoustic wave propagations [10–12]. This inherent robustness renders ALGs particularly advantageous for applications requiring high signal integrity, such as underwater or biomedical environments [13–16]. While current ALGs can achieve specific logic functions with independent modules, a key challenge that remains is the development of acoustic logic networks (ALNs) that integrate multiple logic operations within a single acoustic platform [17–19]. ALNs represent a critical step toward realizing complex acoustic signal processing and computing [20].

The design principle of ALGs typically relies on two main strategies: nonlinear effects and linear interference. Nonlinear effects allow for diverse acoustic operations with simple physical configurations [20]. Linear interference between input and control signals has been employed to develop basic logic gates such as OR and XOR [21,22]. The development of phononic crystals and acoustic metamaterials has significantly facilitated the practical implementation of ALGs [23–26]. However, constructing structurally simple ALGs and integrating them into more compact and versatile computing architectures, i.e., the construction of ALN, remains a promising area for research due to the longer wavelength and weaker interaction of acoustic waves with natural materials.

Recent advancements in nonlocal and non-Hermitian physics provide new theoretical possibilities for enhancing sound-matter interaction in degenerated states [27–29]. These physical mechanisms provide innovative strategies for manipulating sound waves using subwavelength structures [30,31], potentially enabling the realization of multifunctional ALNs. A key feature of non-Hermitian systems

*Contact author: yl@fudan.edu.cn
†Contact author: xuejiang@fudan.edu.cn

is the presence of exceptional points (EPs): singularities in the parameter space where the eigenvalues and corresponding eigenvectors related to a system coalesce [32–35]. This fascinating wave behavior around EPs has led to potential applications in high-sensitivity detection, wireless charging, and quantum information processing [36–39]. In addition, acoustic metagratings, as a special type of gratinglike periodic two-dimensional metamaterial that manipulate wave fronts through tailored diffraction, have been proposed for realizing unidirectional wave propagation, beam splitting, and coherent perfect absorption [40–44]. Therefore, a comprehensive exploration of the nonlocal and non-Hermitian effect in metagratings offers promising solutions to implement the concept of ALNs in a feasible and compact system.

This paper proposes and demonstrates the realization of ALNs based on the nonlocal and non-Hermitian metagratings. The ALN is designed to perform complex logical operations in a simple and compact acoustic platform by utilizing nonlocal interactions within the metagratings and non-Hermitian degenerated states at the EPs. Firstly, we customize the adaptable scattering matrices of the metagratings to realize the diversified control over sound waves. Four types of metagratings are designed through the genetic algorithm, each with a specific EP and scattering matrix. Then, we build the acoustic logic modules (ALMs) by connecting two metagratings. These modules support two input ports for sound waves and an output port for the processed sound, enabling fundamental logical operations such as NOR, OR, XOR, and AND gates. Finally, ALNs of multichannel commuting functions are constructed by cascading different ALMs. We demonstrate the theoretical model, structural optimization, numerical simulations, and experimental validation of the proposed ALNs. Our work highlights the potential of ALNs in future computing architectures by employing nonlocal and non-Hermitian physical mechanisms. This approach could contribute to the development of compact and energy-efficient logic devices with complex digital functionalities.

II. MODEL DESIGN AND RESEARCH METHODS

We start by designing the nonlocal and non-Hermitian metagratings as the basic elements of the ALMs and ALNs. Here, the metagragings operate at the second-order EP to achieve precise control of multiple scattering modes, as illustrated in Fig. 1(a). Each metagrating is composed of periodic subunits containing lossy and lossless grooves. The scattering matrix of the metagraging is designed to control the geometric parameters and losses in the grooves. As shown in Fig. 1(b), an ALM is constructed by connecting two different metagratings, with two input ports for the incident sound waves ($p_{\text{in\_L}}$ and $p_{\text{in\_R}}$) and a processed output port for scattered waves (p_S) in the interactive diamondlike region. Furthermore, an ALN integrating multichannel logical functions is constructed via cascading multiple metagratings, as presented in Fig. 1(c).

A. Design of second-order non-Hermitian metagratings

The manipulation of losses in the grooves of the metagrating plays a critical role in controlling the scattering matrix at the non-Hermitian EPs. For second-order EPs, the non-Hermitian scattering matrix is similar to the Jordan matrix and is denoted as follows [11]:

$$\boldsymbol{S}_{\text{EP}}^2 \sim \boldsymbol{J}^2(E_0) = \begin{bmatrix} E_0 & 1 \\ 0 & E_0 \end{bmatrix}, \tag{1}$$

where E_0 is the degenerated eigenvalue of second-order scattering metagrating. This dual-channel scattering system can generate anomalous reflections at $\pm 45^\circ$ on the incident plane waves, as shown in Fig. 1(a). According to the generalized grating equation, the incident and nth-order reflected waves should satisfy

$$k_0(\sin\theta_r - \sin\theta_i) = nG, \tag{2}$$

where k_0 is the wave number in free space, θ_i and θ_r are, respectively, the incidence and reflection angles, d is the period of metagrating, and $G = 2\pi/d$ is the reciprocal lattice vector. For second-order non-Hermitian metagratings consisting of two input channels, θ_i and θ_r are set to $\pm 45^\circ$. Substituting these into the generalized grating equation, the metagrating period d should satisfy $d = \lambda/\sqrt{2}$. Then, the incident and reflected sound waves are related through the scattering matrix as

$$\begin{bmatrix} p_{\text{re\_R}} \\ p_{\text{re\_L}} \end{bmatrix} = \boldsymbol{S} \begin{bmatrix} p_{\text{in\_L}} \\ p_{\text{in\_R}} \end{bmatrix} = \begin{bmatrix} A_0^L & A_{+1}^R \\ A_{-1}^L & A_0^R \end{bmatrix} \begin{bmatrix} p_{\text{in\_L}} \\ p_{\text{in\_R}} \end{bmatrix}. \tag{3}$$

Here, p is the sound pressure; the subscripts in_ and re_ denote the incidence and reflection, respectively, and L and R mark the directions to the left and right, respectively. The scattering matrix $\boldsymbol{S}$ is composed of reflection coefficients of each scattering mode, with the elements of A_0^L and A_0^R referring to the components on the mirror reflection, whereas A_{-1}^L and A_{+1}^R correspond to the components on retroreflection.

The precise control of the scattering matrix is crucial to the construction of the logical devices. It requires the comprehensive exploration of the nonlocal and complex interactions within the metagratings, which is particularly significant in high-frequency scenarios due to the possible thermoviscous losses and nonlinear effects. Plane sound waves impinging on the boundary of the metagrating will be scattered into different diffraction-order components in various regions of the metagrating, as shown in Fig. 2(a).

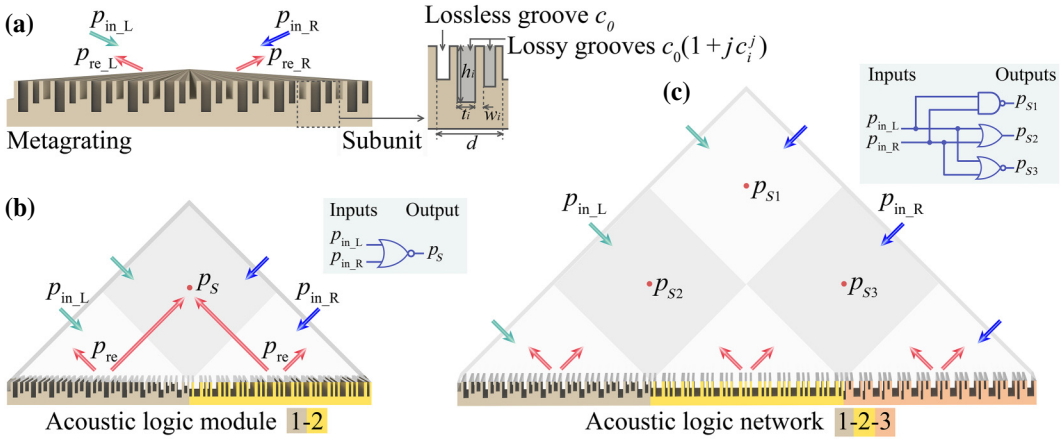

FIG. 1. Schematic diagram of (a) nonlocal and non-Hermitian metagratings, (b) an acoustic logic module (ALM), and (c) an acoustic logic network (ALN). The parameters h_i, t_i, w_i, and c_i^j refer to the depth, width, wall thickness, and loss of the ith groove in the subunit of the metagrating and c_0 is the sound velocity of the background medium. The ALM is built by cascading two different metagratings to perform the basic logical operations such as NOR, OR, XOR, and AND gates. The ALN of multichannel commuting functions is constructed by cascading multiple metagratings. The incident sound waves $p_{\text{in\_L}}$ and $p_{\text{in\_R}}$ operate as two input ports, and the scattered waves p_S (or p_{S1}, p_{S2}, and p_{S3}) in the interactive diamondlike domains are the output ports of different logical functions.

We use the diffraction mode decomposition method to analyze the nonlocal scattering in the metagrating. Sound pressure fields in the free space Field I and grooves of the metagrating Field II can be, respectively, derived as [40]

$$p_{\text{I}}(x,y) = A_0^+ e^{j(-k_0 \sin\theta_i x + + k_0 \cos\theta_i y)} + \sum_n A_n^- e^{-jk_{xn}x} e^{-jk_{yn}y}, \tag{4}$$

$$p_{\text{II}}^i(x,y) = \sum_m [a_{mi}\cos\alpha_{mi}(x-x_i)e^{j\beta_{mi}y} + b_{mi}\cos\alpha_{mi}(x-x_i)e^{-j\beta_{mi}y}]. \tag{5}$$

Here, A_0^+ and A_n^- are the amplitudes of incident waves and the nth-order reflected waves, respectively. In addition, a_{mi} and b_{mi} are the mth-order waveguide mode along the $\mp y$-direction inside the ith groove, with $k \in (1,\ldots,K)$; k_0 is the wave number of incident wave in free space, while $k_{xn} = k_0 \sin\theta_i + nG$ and $k_{yn} = \sqrt{k_0^2 - k_{xn}^2}$ represent the nth-order wave number in the x- and y-direction, respectively, with $n \in (-N,\ldots,0,\ldots,N)$. The complex wave number in the ith lossy groove is modified as $k' = k_0(1+jc_i^j)$. Here, j is the imaginary unit and c_i^j is the imaginary part of the normalized sound velocity representing the energy loss. The loss c_i^j can be adjusted by the thickness of absorbing cotton in practice. Moreover, $\alpha_{mi} = k\pi/t_i$ and $\beta_{mi} = \sqrt{k'^2 - \alpha_{mi}^2}$ are the vibration components in x- and y- direction, respectively, within the ith groove. Both vibration components should satisfy the rigid boundary conditions at $x = x_i$, $x = x_i + t_i$, and $y = -h_i$, where x_i is the initial position of the ith groove. The corresponding velocity along the y-direction is derived as

$$v_y = \frac{1}{-j\rho_0\omega}\frac{\partial p}{\partial y},$$

with ρ_0 and ω being the mass density of the background medium and the angular frequency of the sound waves, respectively. Further applying the continuous conditions of sound pressure and velocity at the boundary between Fields I and II ($y = 0$), we can obtain a linear system of equations related to the amplitude of A_n^- and a_{mi}. Integrating these linear equations and using the genetic algorithm for global optimization, the geometrical parameters and losses in the grooves of the nonlocal metagratings are determined to customize the target scattering matrices. The detailed parameters of four designed metagratings are listed in Table I. These ideal parameters are directly optimized using the genetic algorithm and direct search toolbox (GADS) of MATLAB without considering the actual implementation of the losses in the experiments. The actual parameters of the metagratings fabricated in experiments are modified based on the Johnson-Champoux-Allard model and the optimization module in COMSOL MULTIPHYSICS with MATLAB to accurately implement the loss medium with melamine cotton in practice, that is, c_i^j is achieved by filling melamine cotton with a specific height of l_i in the lossy grooves. The modified parameters are listed in Table II. It should be pointed out that the normalized width and wall thickness of the grooves are restricted to be greater than 0.02 during the optimization process. This avoids creating extremely narrow grooves and thin walls; thereby, the thermoviscous effects and elastic deformation are neglected in our design [40,45]. The

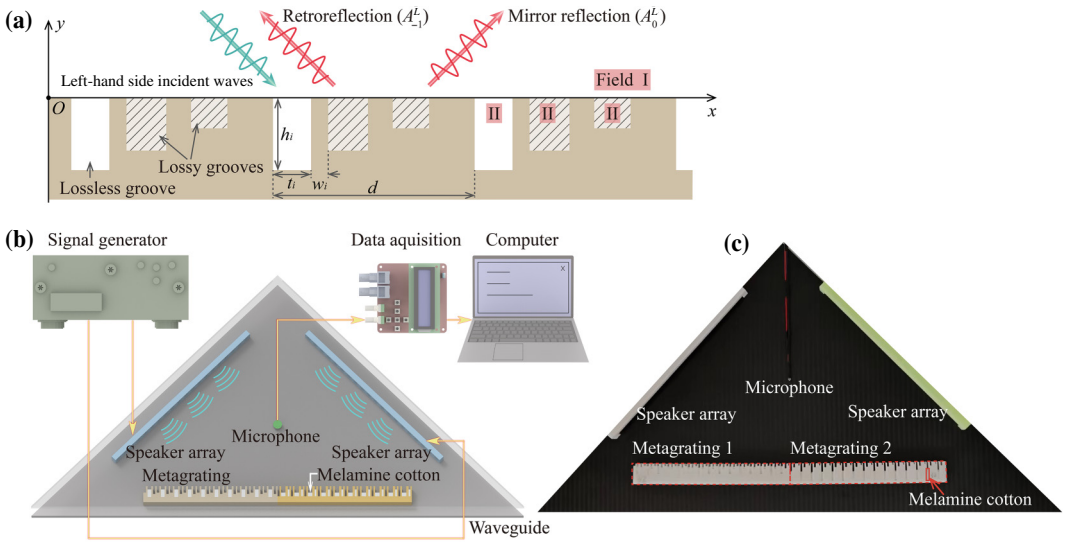

FIG. 2. (a) Coordinate system for metagratings. (b) Schematic and (c) photograph of the experimental setup.

scattering matrix is the optimization objective in the design process, i.e.,

$$\boldsymbol{S}_1 = \begin{bmatrix} 0 & 0 \\ 1 & 0 \end{bmatrix}$$

for metagrating 1,

$$\boldsymbol{S}_2 = \begin{bmatrix} 0 & 1 \\ 0 & 0 \end{bmatrix}$$

for metagrating 2,

$$\boldsymbol{S}_3 = \begin{bmatrix} 0.6 & 0.6 \\ 0 & 0.6 \end{bmatrix}$$

for metagrating 3,

$$\boldsymbol{S}_4 = \begin{bmatrix} 0.35 & 0.35 \\ 0 & 0.35 \end{bmatrix}$$

for metagrating 4.

B. Design of ALMs and ALNs

We further design the ALMs capable of performing different logical operations on the basis of the nonlocal and non-Hermitian metagratings. The metagratings operate as reprogrammable function units to manipulate the distribution of the scattered sound fields. The functionality of the logic system can be tuned by altering the arrangement or modifying the coupling between different metagratings [8,20]. Sound pressure in the interactive diamondlike region is the interference between the sound waves reflected to the right by metagrating 1 and reflected to the left by metagrating 2. Consequently, the scattering matrix $\boldsymbol{S}_{12}$ in the interactive region is derived as [46]

$$\boldsymbol{S}_{12} = \begin{bmatrix} \boldsymbol{S}_1(1,1) & \boldsymbol{S}_1(1,2) \\ \boldsymbol{S}_2(2,1) & \boldsymbol{S}_2(2,2) \end{bmatrix}$$

and the interference sound pressure is calculated by $p_S = p_{\text{re\_R1}} + p_{\text{re\_L2}}$ (subscript 1 or 2 indicates the reflection from metagrating 1 or 2). Therefore, sound waves incident from the left $p_{\text{in\_L}}$ and right $p_{\text{in\_R}}$ operate as the two input ports, and the superimposed sound pressure p_S in the interactive region is the output signal of the logical operation. We consider three input states ($p_{\text{in\_L}} = 1, p_{\text{in\_R}} = 0$), ($p_{\text{in\_L}} = 0, p_{\text{in\_R}} = 1$), and ($p_{\text{in\_L}} = 1, p_{\text{in\_R}} = 1$), and set the threshold of logic binarization to be 0.5; that is, sound pressure p_S with an amplitude larger than 0.5 is considered as logic "1," otherwise it is logic "0." This logic binarization method simplifies the experimental implementation and ensures consistent results across different logical operations. Different logical functions, including the NOR, OR, XOR, and AND gates, can be realized by customizing the scattering matrix of the two connecting metagratings. Furthermore, an ALN of multichannel computing capability is designed via cascading multiple modules, with the scattering matrices in three interactive regions derived as

$$\boldsymbol{S}_{13} = \begin{bmatrix} \boldsymbol{S}_1(1,1) & \boldsymbol{S}_1(1,2) \\ \boldsymbol{S}_3(2,1) & \boldsymbol{S}_3(2,2) \end{bmatrix},$$

$$\boldsymbol{S}_{12} = \begin{bmatrix} \boldsymbol{S}_1(1,1) & \boldsymbol{S}_1(1,2) \\ \boldsymbol{S}_2(2,1) & \boldsymbol{S}_2(2,2) \end{bmatrix},$$

$$\boldsymbol{S}_{23} = \begin{bmatrix} \boldsymbol{S}_2(1,1) & \boldsymbol{S}_2(1,2) \\ \boldsymbol{S}_3(2,1) & \boldsymbol{S}_3(2,2) \end{bmatrix}.$$

TABLE I. Parameters for the metagratings from global optimization.

	ith groove	h_i (λ)	t_i (d)	w_i (d)	c_i^j (c_0)
Metagrating 1	1	0.252	0.189	0.083	0
	2	0.184	0.197	0.123	0.162
	3	0.106	0.182	0.226	0
Metagrating 2	1	0.150	0.111	0.088	0
	2	0.197	0.194	0.102	0.172
	3	0.266	0.185	0.321	0
Metagrating 3	1	0.158	0.211	0.081	0
	2	0.185	0.191	0.192	0.106
	3	0.333	0.115	0.210	0.356
Metagrating 4	1	0.129	0.069	0.097	0
	2	0.245	0.177	0.242	0.328
	3	0.374	0.297	0.117	0.336

C. Numerical model and experimental setup

We carry out numerical simulations and experimental measurements to verify the logical operation performance of the designed metagratings, ALMs and ALNs. The numerical simulations are conducted based on the finite-element method with the software COMSOL MULTIPHYSICS, using the frequency domain module. The mass density and sound velocity of the background medium air are set at $\rho_0 = 1.205$ kg/m^3 and $c_0 = 343$ m/s. All the boundaries of the grooves are chosen to be rigid, and boundaries of the calculation domain are set as perfectly matched layers to reduce the reflection from the outside. Plane-wave incident conditions are applied to the input ports. We use the parameters of the metagratings listed in Table I for the simulations. Monochromatic sound waves of 20 kHz (wavelength $\lambda = 17.15$ mm) are used in both the simulations and experiments.

The experimental setup resembles the simulations. The measurements are conducted in a two-dimensional waveguide constructed with two carbon fiber-reinforced plastics, as shown in Figs. 2(b) and 2(c). The height of the waveguide is fixed at 8.5 mm (smaller than half wavelength) to guarantee the plane-wave mode inside the waveguide. The samples of metagratings are made of photosensitive resin (mass density 1180 kg/m^3 and sound velocity 2250 m/s, with acoustic impedance 6423 times larger than air) and fabricated with 3D printing technology. Each metagrating is composed of 15 subunits arranged periodically, with one or two grooves in each unit filled with melamine cotton with a specific height of l_i^{cotton} to generate the desired non-Hermitian scattering matrix. Using 15 subunits ensures that the metagratings approach infinite periodicity while reducing edge effects. The physical parameters of the four fabricated metagratings are listed in Table II. We fabricated two speaker arrays positioned on two boundaries to generate the incident plane waves $p_{\text{in\_L}}$ and $p_{\text{in\_R}}$ inside the waveguide. The incident angles are fixed at $\pm 45^\circ$. Melamine cotton is also deployed on the boundaries of the waveguide to minimize the reflection and environmental noise. A mini microphone (GMI3015L50-2C30-66DB) maneuvered by a 3D scanning stage is employed to measure the sound pressure field, with 3 mm spacing between each point. The time-dependent signal is captured through data acquisition hardware (NI DAQ-9174) and processed with a computer. The temporal signal is analyzed with a Fourier transform to extract the amplitude and phase information of the sound waves at 20 kHz. The scattered sound pressure field is obtained by subtracting the incident field without metagratings from the total sound fields with metagratings.

TABLE II. Parameters for the metagratings fabricated in the experiments.

	ith groove	h_i (λ)	t_i (d)	w_i (d)	l_i^{cotton} (λ)
Metagrating 1	1	0.252	0.189	0.083	0
	2	0.675	0.132	0.188	0.410
	3	0.106	0.182	0.226	0
Metagrating 2	1	0.150	0.111	0.088	0
	2	1.188	0.167	0.129	0.675
	3	0.266	0.185	0.321	0
Metagrating 3	1	0.158	0.211	0.081	0
	2	0.752	0.129	0.254	0.418
	3	0.298	0.199	0.125	0.170
Metagrating 4	1	0.129	0.069	0.097	0
	2	0.697	0.123	0.296	0.375
	3	0.717	0.144	0.270	0.321

III. RESULTS AND DISCUSSION

A. Performance of individual metagratings at second-order EPs

We first demonstrate the performance of individual metagratings in the simulations and experiments, as shown in Fig. 3. Four different metagratings are investigated in this section, each of which is designed independently with different EPs. The green arrow represents incident waves from the left $p_{\text{in\_L}}$ with $\theta_i = +45^\circ$, and the blue arrow denotes incident waves from the right $p_{\text{in\_R}}$ with $\theta_i = -45^\circ$. The scattered sound fields are normalized with respect to the incident sound pressure amplitude. For metagrating 1 in Figs. 3(a1) and 3(a2), the scattering matrix is given as

$$\boldsymbol{S}_1 = \begin{bmatrix} 0 & 0 \\ 1 & 0 \end{bmatrix}.$$

The incident sound waves from the left retroreflect perfectly on metagrating 1, whereas the incident sound waves from the right are suppressed completely. Figures 3(b1) and 3(b2) exhibit that the left-hand side incident sound

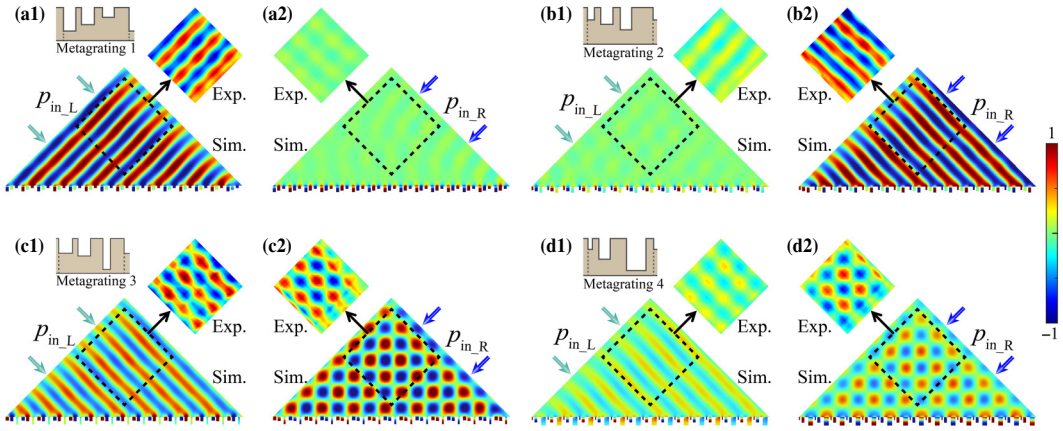

FIG. 3. Numerical simulations and experimental demonstration of the precise sound manipulation with the nonlocal and non-Hermitian metagratings. Scattered sound fields of (a1, a2) metagrating 1, (b1, b2) metagrating 2, (c1, c2) metagrating 3, and (d1, d2) metagrating 4. Each metagrating is designed with a particular scattering matrix.

waves are suppressed completely on metagrating 2 with

$$\boldsymbol{S}_2 = \begin{bmatrix} 0 & 1 \\ 0 & 0 \end{bmatrix},$$

while the right-hand side incident sound waves retroreflect perfectly. Moreover, the scattering matrix of metagrating 3

$$\boldsymbol{S}_3 = \begin{bmatrix} 0.6 & 0.6 \\ 0 & 0.6 \end{bmatrix}$$

indicates that the left-hand side incident waves are mirror-reflected with a reflection coefficient of 0.6, while the right-hand side incident waves are mirror-reflected and retroreflected with the same reflection coefficient of 0.6, as shown in Figs. 3(c1) and 3(c2). The reflection coefficient is defined as the normalized ratio between amplitudes of the scattered and incident sound pressure. Figures 3(d1) and 3(d2) show that the scattering field of metagrating 4 with

$$\boldsymbol{S}_4 = \begin{bmatrix} 0.35 & 0.35 \\ 0 & 0.35 \end{bmatrix},$$

is similar to that of metagrating 3, except that the reflection coefficient is reduced from 0.6 to 0.35 [40]. Good agreements are observed from the simulation and experimental results, all of which verify that the nonlocal and non-Hermitian metagratings can precisely control the sound wave propagation according to the desired scattering matrices, providing a solid foundation for the construction of the ALMs and ALNs capable of more complex logical operations.

B. Performance of ALMs for basic logical operation

The performance of ALMs composed of two different metagratings from the simulations and experiments are summarized in Fig. 4. We construct four ALMs labeled as ALM 1-2 (sequential combination of metagrating 1 and metagrating 2), ALM 2-1, ALM 3-2, and ALM 4-2 from Figs. 4(a)–4(d), which are capable of performing the NOR, OR, XOR, and AND logical functions, respectively. For example, sound pressure in the interactive area of ALM 1-2 in Fig. 4(a) is the interference between the sound pressure reflected to the right by metagrating 1 and to the left by metagrating 2. Consequently, the scattering matrix in the interactive region $\boldsymbol{S}_{12}$ is equal to $\begin{bmatrix} 0 & 0 \\ 0 & 0 \end{bmatrix}$, which indicates that both the left- and right-hand side incident sound waves will be completely suppressed at the output. Figures 4(a1)–4(a3) exhibit the scattered sound pressure fields in three different input states from the simulations and experiments, where the scattered signals in the interactive region nearly vanish in spite of different incident conditions. For a clear comparison, we extract the measured temporal sound pressure signals in the two input ports and at the center point of the interactive region, as shown in Fig. 4(a4). The outputs in all three different input states are logic "0," proving that the designed ALM 1-2 performs the NOR logical function. The light-gray regions in Figs. 4(a4)–4(d4) show the threshold value 0.5 of logic binarization in each device. The results of ALM 2-1 with

$$\boldsymbol{S}_{21} = \begin{bmatrix} 0 & 1 \\ 1 & 0 \end{bmatrix}$$

are displayed in Fig. 4(b). In this situation, both the left- and right-hand side incident sound waves completely retroreflect into the interactive region, resulting in the constructive interference of p_S. Therefore, the output of p_S is logic "1" under all input states, as shown in Fig. 4(b4), which proves that ALM 2-1 performs the OR logical function. In addition, the scattering matrices of ALM 3-2 in

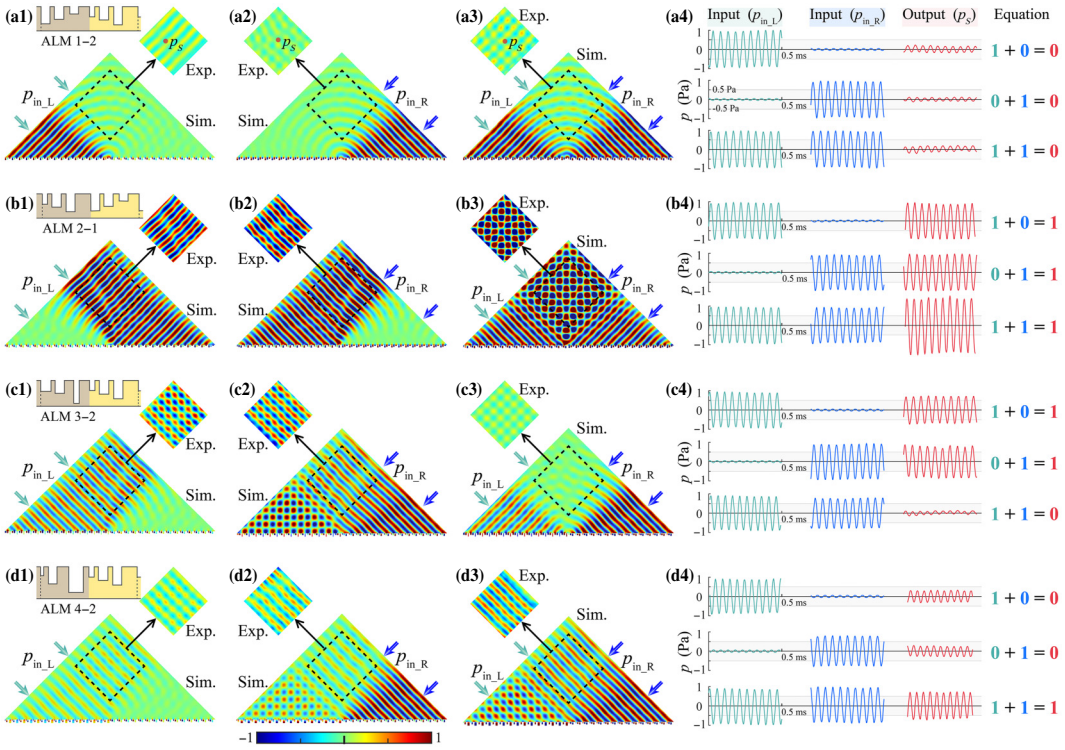

FIG. 4. Numerical simulations and experimental demonstration of ALMs capable of different logical functions. Scattered sound fields of (a1, a2, a3, a4) ALM 1-2, (b1, b2, b3, b4) ALM 2-1, (c1, c2, c3, c4) ALM 3-2, and (d1, d2, d3, d4) ALM 4-2, which perform the logical operation functions for NOR, OR, XOR, and AND gates, respectively. The temporal signals of the incident and scattered sound waves (at the central point of the dashed box) extracted from the experiments show the logical relationship among the two input ports and one output port of the designed ALMs.

Fig. 4(c) and ALM 4-2 in Fig. 4(d) are

$$\boldsymbol{S}_{32} = \begin{bmatrix} 0.6 & 0.6 \\ 0 & 0 \end{bmatrix} \quad \text{and} \quad \boldsymbol{S}_{42} = \begin{bmatrix} 0.35 & 0.35 \\ 0 & 0 \end{bmatrix},$$

respectively. The left-hand side incident sound waves are mirror-reflected to the right, while the right-hand side incident sound waves are retroreflected in both ALM 3-2 and ALM 4-2. Therefore, when sound waves incident from the left or right independently, the reflection coefficient in the interactive region is 0.6 for ALM 3-2 and 0.35 for ALM 4-2, and the output signal is logic "1" and logic "0," respectively. However, for simultaneous incidence from both the left and right directions, the scattered signal is the coherent superimposition of mirror reflection from left-hand side incidence and retroflection for right-hand side incidence. For ALM 3-2, the two incident sound waves are set as out-phase, and the output is $p_S = 0.6 - 0.6 = 0$. Therefore, the outputs of ALM 3-2 under three input states are logic "1," "1," and "0," which characterizes the function of the XOR logic gate of ALM 3-2. For ALM 4-2, the two incident waves are set as in-phase, and the scattered signal $p_S = 0.35 + 0.35 = 0.7$ gives the output logic "1." Consequently, ALM 4-2 forms an AND logic gate with the outputs of logic "0," "0," and "1" under three input states. ALMs of more versatile logical operations can be realized by utilizing the linear interference of scattered sound waves from different combinations of metagratings in the interactive region.

C. Performance of ALNs for multichannel computing

The ALMs can be used as the basic building blocks to realize more complex Boolean logic and algorithms, owning to the independent and precise manipulation of the scattering matrix based on the second-order nonlocal and non-Hermitian metagratings. We construct two different ALNs of multichannel computing functionalities, each of which has two input ports and three output ports performing different logical operations. ALN 3-1-2 is the sequential combination of ALM 3-1 and ALM 1-2, with the scattering matrices in three interactive regions being

$$\boldsymbol{S}_{32} = \begin{bmatrix} 0.6 & 0.6 \\ 0 & 0 \end{bmatrix}, \quad \boldsymbol{S}_{31} = \begin{bmatrix} 0.6 & 0.6 \\ 1 & 0 \end{bmatrix}, \quad \text{and}$$

$$\boldsymbol{S}_{12} = \begin{bmatrix} 0 & 0 \\ 0 & 0 \end{bmatrix}.$$

The scattered sound fields under the individual incidence from the left- or right-hand side and the simultaneous

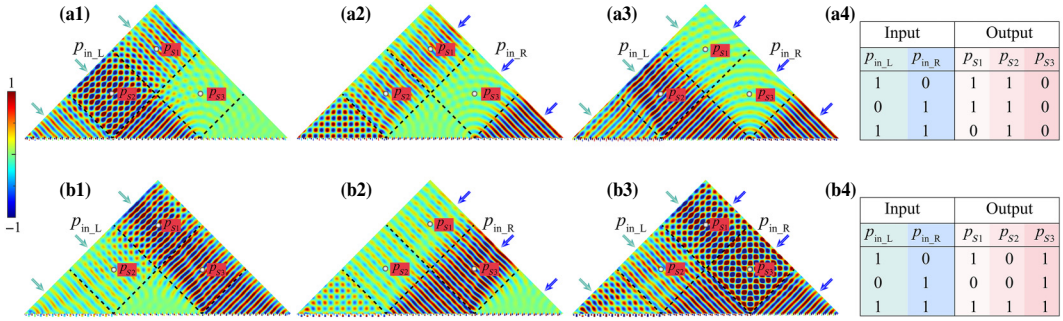

FIG. 5. Performance of ALNs for multichannel logic computing. Scattered sound fields and truth table of (a1, a2, a3, a4) ALN 3-1-2 and (b1, b2, b3, b4) ALN 4-2-1. The values in the truth table are extracted from the sound pressure at the positions indicated by white dots in the fields.

out-phase incidence from both sides are shown in Figs. 5(a1)–5(a3), and the truth table of logic outputs in different channels are plotted in Fig. 5(a4). These three output ports of p_{S1}, p_{S2}, and p_{S3} present the logical operation functions of XOR, OR, and NOR, respectively. The performance of another ALN 4-2-1 is shown in Fig. 5(b). The scattering matrices in three output regions are

$$\boldsymbol{S}_{41} = \begin{bmatrix} 0.35 & 0.35 \\ 1 & 0 \end{bmatrix}, \quad \boldsymbol{S}_{42} = \begin{bmatrix} 0.35 & 0.35 \\ 0 & 0 \end{bmatrix}, \quad \text{and}$$

$$\boldsymbol{S}_{21} = \begin{bmatrix} 0 & 1 \\ 1 & 0 \end{bmatrix},$$

respectively. For this device, the incident sound waves from the left- and right-hand sides are set as in-phased. As shown in the truth table in Fig. 5(b4), the output ports of p_{S2} and p_{S3} indicate the logical operation functions of AND and OR. The logic value of output p_{S1} is equal to that of the left-hand side incident sound waves $p_{\text{in\_L}}$, but independent in relation to the right-hand side incident sound waves $p_{\text{in\_R}}$. The ALNs integrate the functionality and independence of the basic logic gates of ALMs, demonstrating the potential of multichannel logic computing realized in a compact and simple acoustic platform.

IV. CONCLUSION

This study proposed the concept and demonstrated the implementation of ALNs that integrate multiple acoustic logic operations. A nonlocal and non-Hermitian metagrating has been designed and applied as a functional unit for processing acoustic information and activating various acoustic logic gates and logic circuits. The scattering matrices of different metagratings operating at the second-order EPs are customized by optimizing the geometrical and absorption parameters of the grooves. The results from theoretical calculations, numerical simulations, and experimental measurements consistently verify the performance of an individual metagrating, with different logical functions of ALMs and multichannel computing capability of ALNs. Four ALMs with distinctive logical operation functions of NOR, OR, XOR, and AND logic gates and two ALNs with three ports computing outputs have been realized. ALNs integrate the functionality and independence of the basic logic operation of ALMs, enhancing computational density and reducing the physical footprint of logic devices. This integration promotes a paradigm shift in acoustic computing, potentially overcoming limitations faced by electronic and optical computing systems, particularly in environments adverse to electronic interference or where miniaturization is paramount.

Recognizing the fundamental advantages of ALNs for logic gates and computing circuits, we envision further development of the concept as follows. (i) Variable incident waves. Currently, the incident sound waves on the metagrating are plane waves. By designing wave profiles of sound along the incident boundary (amplitude, phase, wavelength, etc.), more versatile acoustic logic gates and signal processing driven by ALNs are realizable. (ii) Transient logic operations. Currently, all the devices are driven by stable input signals. Transient logical operations could be achieved by applying the time-dependent input signal. (iii) Complex functional units. This study uses the relatively simple second-order reflection-type metagratings as functional units. Exploring the design of higher-order or other more complex functional units and implementing logic cascades holds great promise for future advancements.

ACKNOWLEDGMENTS

This work is supported by the National Key R&D Program of China (Grant No. 2023YFA1407800), the National Natural Science Foundation of China (Grants No. T2222024 and No. 12034005), the STCSM Science and Technology Innovation Plan of Shanghai Science and Technology Commission (Grant No. 21JC1400300), the Shuguang Program supported by the Shanghai Education Development Foundation, and the Shanghai Municipal

Education Commission. X.J. acknowledges support from the Xiaomi Young Talents Program.

The authors declare that they have no known competing financial interests or personal relationships that could have influenced the work reported in this paper.

[1] L. He, D. Liu, J. Gao, W. Zhang, H. Zhang, X. Feng, Y. Huang, K. Cui, F. Liu, W. Zhang, and X. Zhang, Super-compact universal quantum logic gates with inverse-designed elements, Sci. Adv. **9**, 6685 (2023).

[2] P. V. Klimov, *et al.*, Optimizing quantum gates towards the scale of logical qubits, Nat. Commun. **15**, 2442 (2024).

[3] Z. Zhou, J. Wang, R. D. Levine, F. Remacle, and I. Willner, DNA-based constitutional dynamic networks as functional modules for logic gates and computing circuit operations, Chem. Sci. **12**, 5473 (2021).

[4] P. Jin, J. Fu, F. Wang, Y. Zhang, P. Wang, X. Liu, Y. Jiao, H. Li, Y. Chen, Y. Ma, and X. Feng, A flexible, stretchable system for simultaneous acoustic energy transfer and communication, Sci. Adv. **7**, 2507 (2021).

[5] H. Xiao, T. Li, L. Zhang, W.-H. Liao, T. Tan, and Z. Yan, Metamaterial based piezoelectric acoustic energy harvesting: Electromechanical coupled modeling and experimental validation, Mech. Syst. Signal Process. **185**, 109808 (2023).

[6] H. Xiao, T. Tan, T. Li, L. Zhang, C. Yuan, and Z. Yan, Enhanced multi-band acoustic energy harvesting using double defect modes of Helmholtz resonant metamaterial, Smart Mater. Struct. **32**, 105030 (2023).

[7] Z.-x. Chen, L.-l. Ma, S.-j. Ge, Z.-G. Chen, M.-h. Lu, Y.-f. Chen, and Y.-q. Lu, Transient logic operations in acoustics through dynamic modulation, Phys. Rev. Appl. **21**, L011001 (2024).

[8] J. Lan, L. Wang, X. Zhang, M. Lu, and X. Liu, Acoustic multifunctional logic gates and amplifier based on passive parity-time symmetry, Phys. Rev. Appl. **13**, 034047 (2020).

[9] T. Zhang, Y. Cheng, J.-z. Guo, J.-y. Xu, and X.-j. Liu, Acoustic logic gates and Boolean operation based on self-collimating acoustic beams, Appl. Phys. Lett. **106**, 113503 (2015).

[10] X. Fang, N. J. R. K. Gerard, Z. Zhou, H. Ding, N. Wang, B. Jia, Y. Deng, X. Wang, Y. Jing, and Y. Li, Observation of higher-order exceptional points in a nonlocal acoustic metagrating, Commun. Phys. **4**, 271 (2021).

[11] X. Fang, N. Wang, W. Wu, W. Wang, X. Yin, X. Wang, and Y. Li, Extreme wave manipulation via non-hermitian metagratings on degenerated states, Phys. Rev. Appl. **19**, 054003 (2023).

[12] C. Vanhille and C. Campos-Pozuelo, An acoustic switch, Ultrason. Sonochem. **21**, 50 (2014).

[13] A. Nowbahari, L. Marchetti, and M. Azadmehr, Low power wake-up receivers for underwater acoustic wireless sensor networks, IEEE Trans. Green Commun. Netw. **7**, 1635 (2023).

[14] A. Sanchez, S. Blanc, P. Yuste, and J. J. Serrano, A low cost and high efficient acoustic modem for underwater sensor networks, in *OCEANS 2011 IEEE - Spain* (2011), pp. 1–10.

[15] P. Zhang, T. Li, J. Zhu, X. Zhu, S. Yang, Y. Wang, X. Yin, and X. Zhang, Generation of acoustic self-bending and bottle beams by phase engineering, Nat. Commun. **5**, 4316 (2014).

[16] H. T. Zhou, M. Jiang, J. H. Zhu, Y. Li, Q. Li, Y. F. Wang, C. W. Qiu, and Y. S. Wang, Underwater scattering exceptional point by metasurface with fluid-solid interaction, Adv. Funct. Mater. 2404282 (2024).

[17] F. H. Asgharkhani and A. Bahrami, Four-input acoustic XOR logic gate based on solid-solid phononic crystals, Fundam. Appl. **57**, 101192 (2023).

[18] T. Zhang, Y. Cheng, B.-G. Yuan, J.-Z. Guo, and X.-J. Liu, Compact transformable acoustic logic gates for broadband complex Boolean operations based on density-near-zero metamaterials, Appl. Phys. Lett. **108**, 183508 (2016).

[19] C.-y. Zuo, J.-p. Xia, H.-x. Sun, Y. Ge, S.-q. Yuan, and X.-j. Liu, Broadband acoustic logic gates in a circular waveguide with multiple ports, Appl. Phys. Lett. **111**, 243501 (2017).

[20] F. Li, P. Anzel, J. Yang, P. G. Kevrekidis, and C. Daraio, Granular acoustic switches and logic elements, Nat. Commun. **5**, 5311 (2014).

[21] Y.-J. Lu, Y. Ge, S.-Q. Yuan, H.-X. Sun, and X.-J. Liu, Acoustic logic gates by a curved waveguide with ultrathin metasurfaces, J. Phys. D: Appl. Phys. **53**, 015301 (2020).

[22] Y. Wang, J. P. Xia, H. X. Sun, S. Q. Yuan, and X. J. Liu, Binary-phase acoustic passive logic gates, Sci. Rep. **9**, 8355 (2019).

[23] S. Bringuier, N. Swinteck, J. O. Vasseur, J. F. Robillard, K. Runge, K. Muralidharan, and P. A. Deymier, Phase-controlling phononic crystals: realization of acoustic Boolean logic gates, J. Acoust. Soc. Am. **130**, 1919 (2011).

[24] Y. Li, K. Huang, M. Gong, C. Sun, S. Gao, Y. Lai, and X. Liu, Realization of acoustic tunable logic gate composed of soft materials, Results Phys. **57**, 107421 (2024).

[25] Y.-j. Lu, Y. Wang, Y. Ge, S.-q. Yuan, D. Jia, H.-x. Sun, and X.-j. Liu, Multifunctional acoustic logic gates by valley sonic crystals, Appl. Phys. Lett. **121**, 123506 (2022).

[26] J. P. Xia, D. Jia, H. X. Sun, S. Q. Yuan, Y. Ge, Q. R. Si, and X. J. Liu, Programmable coding acoustic topological insulator, Adv. Mater. **30**, e1805002 (2018).

[27] X. Wang, R. Dong, Y. Li, and Y. Jing, Nonlocal and non-Hermitian acoustic metasurfaces, Rep. Prog. Phys. **86**, 116501 (2023).

[28] H. Xie and Z. Hou, Nonlocal metasurface for acoustic focusing, Phys. Rev. Appl. **15**, 034054 (2021).

[29] L. Zhang, Y. Yang, Y. Ge, Y. J. Guan, Q. Chen, Q. Yan, F. Chen, R. Xi, Y. Li, D. Jia, S. Q. Yuan, H. X. Sun, H. Chen, and B. Zhang, Acoustic non-Hermitian skin effect from twisted winding topology, Nat. Commun. **12**, 6297 (2021).

[30] X. Wang, A. Díaz-Rubio, and S. A. Tretyakov, Independent control of multiple channels in metasurface devices, Phys. Rev. Appl. **14**, 024089 (2020).

[31] B. Wu, W. Jiang, J. Jiang, Z. Zhao, Y. Tang, W. Zhou, and W. Chen, Wave manipulation in intelligent metamaterials: Recent progress and prospects, Adv. Funct. Mater. **4**, 2316745 (2024).

[32] Z. Hou, X. Fu, and Y. Liu, Singularity of the Bloch theorem in the fluid/solid phononic crystal, Phys. Rev. B **73**, 024034 (2006).

[33] A. Iyer, Y. P. Kandel, W. Xu, J. M. Nichol, and W. H. Renninger, Coherent optical coupling to surface acoustic wave devices, Nat. Commun. **15**, 3993 (2024).

[34] Z.-K. Lin, Q. Wang, Y. Liu, H. Xue, B. Zhang, Y. Chong, and J.-H. Jiang, Topological phenomena at defects in acoustic, photonic and solid-state lattices, Nat. Rev. Phys. **5**, 483 (2023).

[35] X. Wang, X. Fang, D. Mao, Y. Jing, and Y. Li, Extremely asymmetrical acoustic metasurface mirror at the exceptional point, Phys. Rev. Lett. **123**, 214302 (2019).

[36] K. Bai, L. Fang, T. R. Liu, J. Z. Li, D. Wan, and M. Xiao, Nonlinearity-enabled higher-order exceptional singularities with ultra-enhanced signal-to-noise ratio, Natl. Sci. Rev. **10**, nwac259 (2023).

[37] Z. Dong, Z. Li, F. Yang, C.-W. Qiu, and J. S. Ho, Sensitive readout of implantable microsensors using a wireless system locked to an exceptional point, Nat. Electron. **2**, 335 (2019).

[38] H. Hodaei, A. U. Hassan, S. Wittek, H. Garcia-Gracia, R. El-Ganainy, D. N. Christodoulides, and M. Khajavikhan, Enhanced sensitivity at higher-order exceptional points, Nature **548**, 187 (2017).

[39] Z. Li, C. Li, Z. Xiong, G. Xu, Y. R. Wang, X. Tian, X. Yang, Z. Liu, Q. Zeng, R. Lin, Y. Li, J. K. W. Lee, J. S. Ho, and C. W. Qiu, Stochastic exceptional points for noise-assisted sensing, Phys. Rev. Lett. **130**, 227201 (2023).

[40] S. Cao and Z. Hou, Angular-asymmetric transmitting metasurface and splitter for acoustic waves: Combining the coherent perfect absorber and a laser, Phys. Rev. Appl. **12**, 064016 (2019).

[41] Y. Fu, C. Shen, Y. Cao, L. Gao, H. Chen, C. T. Chan, S. A. Cummer, and Y. Xu, Reversal of transmission and reflection based on acoustic metagratings with integer parity design, Nat. Commun. **10**, 2326 (2019).

[42] Y. Fu, C. Shen, X. Zhu, J. Li, Y. Liu, S. A. Cummer, and Y. Xu, Sound vortex diffraction via topological charge in phase gradient metagratings, Sci. Adv. **6**, eaba9876 (2024).

[43] Y. Hu, Z. B. Lin, Z. L. Li, Y. G. Peng, and X. F. Zhu, Experimental investigation of acoustic moire effect controlled by twisted bilayer gratings, Ultrasonics **141**, 107338 (2024).

[44] X. Kuci, M. G. D. Geers, and V. G. Kouznetsova, Towards design of a gradient locally resonant acoustic metasurface for negative reflection, J. Mech. Phys. Solids **187**, 105632 (2024).

[45] M. Bruneau, *Fundamentals of Acoustics* (John Wiley & Sons, London, 2013).

[46] A. J. Berkhout, D. de Vries, and P. Vogel, Acoustic control by wave field synthesis, J. Acoust. Soc. Am. **93**, 2764 (1993).